J. Fluid Mech. (2024), *vol*. 1000, A14, doi:10.1017/jfm.2024.990

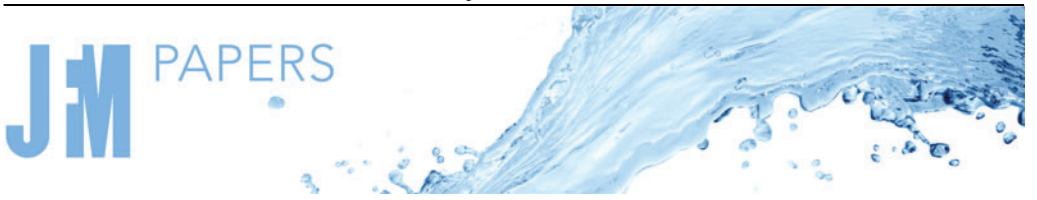

On the transition in spanwise wake instability characteristics behind oscillating foils

Suyash Verma[1] **and Arman Hemmati**[1],†

[1]Department of Mechanical Engineering, University of Alberta, Edmonton, AB, Canada T6G 2R3

(Received 15 December 2023; revised 15 August 2024; accepted 10 October 2024)

Spanwise vortex instability and the growth of secondary hairpin-like vortical structures in the wake of an oscillating foil are investigated numerically at Reynolds number 8000 in a range of chord-based Strouhal number ($0.32 \leq St_c \leq 0.56$). The phase-offset (ϕ) between the heaving and pitching motion is $\phi = 90^\circ$. The wake at the lowest St_c (0.32) is characterized by a single system of streamwise hairpin-like structures that evolve from the core vorticity outflux of the secondary leading edge vortex (LEV) over the foil boundary. The primary LEV features spanwise dislocations, but it does not reveal substantial changes advecting downstream. Increasing St_c beyond 0.32 reveals that the transition in spanwise instability characterizes the deformation of primary LEV cores, which subsequently transforms to hairpin-like secondary structures. At higher St_c, stronger trailing edge vortices (TEVs) grow in close proximity to the primary LEVs, which contributes to an enhanced localized vortex compression and tilting near dislocations. This phenomenon amplifies the undulation amplitude of primary LEVs, eventually leading to vortex tearing. The larger circulation of TEVs with increasing St_c provides an additional explanation for an accelerated vortex compression that coincides with a faster transition of spanwise LEV instability to secondary hairpin-like structures in the wake.

Key words: swimming/flying, vortex dynamics, wakes

1. Introduction

Unsteady dynamics of leading edge vortices (LEVs) has a considerable influence on the operation of bio-inspired robotic swimmers and micro underwater vehicles (Mueller & DeLaurier 2003). Spanwise instability of LEVs promotes the growth of secondary hairpin-like structures that eventually lead to wake three-dimensionality (Verma, Khalid & Hemmati 2023). Understanding mechanisms of the spatio-temporal dynamics of such

† Email address for correspondence: arman.hemmati@ualberta.ca

instabilities is important, since they directly influence the force and rolling moments generated on the lifting surface of wings, for example (Chiereghin *et al.* 2020). As the LEVs advect along the oscillating body, spatio-temporal changes in vortex instability impose variations in aerodynamic and hydrodynamic moments. This directly impacts the vibration and structural integrity of the body (Bull *et al.* 2021). This also includes aspects of controllability, which is crucial in the case of small-scale micro air vehicles and autonomous underwater vehicles that warrant rapid response from the control systems (Visbal 2012). Disintegration of vortex structures in the wake of oscillating foils also holds importance for understanding mechanisms that can reduce noise generation. This is observed during motion of helicopter rotor and wind turbine blades, where their high frequency flutter closely resembles an oscillatory motion of a solid body (Wang, Zhao & Wu 2015). In certain conditions, undesirable effects of dynamic stall and noise can be prevented by artificially imposing oscillations that promote growth of vortex instability and its faster disintegration (Zurman-Nasution, Ganapathisubramani & Weymouth 2020; Talboys *et al.* 2021). Instability characterization also helps in establishing an association between unsteady vortex dynamics and propulsive performance of swimming mammals (Deng & Caulfield 2015; Deng *et al.* 2016; Sun, Deng & Shao 2018; Verma & Hemmati 2021). Recently, transition of spanwise instability of LEVs to secondary hairpin-like structures is also reported for flows over biological oscillating fins of batoids (Zhang & Huang 2023). This study revealed the development of spanwise corrugations on LEVs, which subsequently curl into streamwise vorticity filaments. These filaments, under increased strain fields of vortex cores, are stretched to form one-legged hairpin structures (Zhang & Huang 2023). The pectoral fin experienced a stronger and faster LEV deformation, ultimately contributing to the formation of hairpin-like vortex arrangement. This was due to its higher amplitude compared to the rest of the body. Verma & Hemmati (2023) provided elaborate description of the evolution features of secondary instabilities and intermediate secondary hairpin-like structures at phase-offset $90^\circ \leq \phi \leq 270^\circ$ and Strouhal number $St_c = 0.32$. This study extends the findings of Verma & Hemmati (2023) by assessing the influence of varying St_c on the transition in primary LEV instability and subsequent transformation to secondary hairpin-like structures.

Elliptic instability has been linked primarily to pairs of spanwise coherent structures, known as rollers, rotating in counter directions with either equal or unequal strength (Leweke & Williamson 1998; Ortega & Savas 2001; Leweke, Le Dizès & Williamson 2016). Both experimental and numerical investigations modelling such instabilities have concentrated on isolated pairs of vortices. In these studies, temporal evolution of the spatial dislocations on the rollers has been observed clearly (Leweke & Williamson 1998; Bristol *et al.* 2004). Ortega, Bristol & Savas (2003) conducted a stability analysis on paired vortices, and provided a quantitative assessment involving circulation, internal strain field distribution, and evolution mechanisms of sinusoidal instability. These revealed a spatial wavelength of lower magnitude compared to Crow's estimation for an equal-strength vortex pair (Crow 1970). Bristol *et al.* (2004) extended existing analysis to a co-rotating vortex pair, illustrating the formation of vorticity bridges due to elliptic instability, contributing to vortex merger in the wake. Meunier & Leweke (2005) also revealed that Crow's linear stability model effectively characterizes the behaviour of equal-strength counter-rotating vortex pairs, showing that the early growth phase of instability aligns with vortex pair merger at specific spanwise intervals, resulting in a vortex ring-like arrangement.

In addition to the foundational investigations on spanwise instabilities of isolated vortex pairs, their impact on the wake three-dimensionality has been noted previously in the

context of stationary bluff bodies. Examples include a circular cylinder (Barkley & Henderson 1996; Brede, Eckelmann & Rockwell 1996; Williamson 1996) and a blunt trailing edge aerofoil (Ryan, Thompson & Hourigan 2005; Gibeau, Koch & Ghaemi 2018). Experimental visualizations have indicated that the development of streamwise coherent structures, referred to as ribs, is linked to spanwise instability modes exhibiting distinct spatio-temporal characteristics (Williamson 1996). Mittal & Balachandar (1995) emphasized the emergence of secondary hairpin-like configurations, which manifested as spatial dislocations along the spanwise rollers downstream of a stationary circular cylinder. Over time, these displaced formations extended and gave rise to rib pairs. Thus Mittal & Balachandar (1995) and Williamson (1996) conclusively affirmed the crucial role of intermediary structures in the formation of three-dimensional wake features.

Fluid dynamicists have broadened their examination of instability beyond stationary bluff bodies. This involves assessing instability in rigid bodies engaged in prescribed oscillations (Nazarinia *et al.* 2009; Visbal 2009; Deng & Caulfield 2015; Sun *et al.* 2018). These studies delve into diverse facets of secondary wake structures, and elucidate their impact on three-dimensional characteristics of the wake. Visbal (2009) emphasized a substantial influence of varying St_c on the behaviour of LEVs. Notably, higher St_c values were observed to contribute towards significant deformations of the LEV, ultimately transitioning it into an arched vortex undulation pattern that was noted by Visbal (2009) and Calderon *et al.* (2014). The presence of instability modes with varying wavelengths, both long and short, and the resulting arrangement of secondary vortices, were investigated on a pitching foil by Deng & Caulfield (2015). This revealed a direct correlation between the formation of secondary vortex pairs and the asymmetric arrangement of primary rollers shed behind the foil. Moriche, Flores & García-Villalba (2016) conducted stability analysis on a foil with combined heaving and pitching motion, which provided insights into the three-dimensional wake transition and its impact on aerodynamic forces. Although there were minimal effects on forces, simulations revealed that the onset of three-dimensionality for the wake of infinite-span oscillating wings was associated with the bending of the trailing edge vortex (TEV) (Moriche *et al.* 2016). Oscillating foils governed by both pitching and heaving motion also present a better performance in energy harvesting systems (Kim *et al.* 2017). For a purely heaving motion, the LEV can possibly separate from the foil boundary, which subsequently coincides with a sudden drop in lift force. To counter this, a pitching motion can be added to the foil that rotates it effectively to produce another LEV. This balances the power loss resulting from the separation of the LEV in the previous half shedding cycle. Such benefits have also been confirmed for biological locomotion of animals (Kim *et al.* 2017).

Chiereghin *et al.* (2020) identified sinusoidal undulation on the shed LEV filament in the wake of a high aspect ratio heaving swept wing. The origins of these undulations remained unclear, speculated to be an instability of oscillating shear flow, the mixing layer, or the vortex filament itself. Additionally, Chiereghin *et al.* (2020) noted that increasing circulation of LEVs at high reduced frequencies (k) resulted in stronger deformations, coinciding with significant effects on lift and bending moments. Verma & Hemmati (2021) highlighted the prevalence of elliptic-type short-wavelength instability in highly propulsive wake flows, as discussed originally by Leweke & Williamson (1998). Further evidence was also presented on the emergence of tongue-like dislocations on the primary rollers at low St_c. However, wakes associated with high St_c and larger thrust generation exhibited interconnected hairpin–horseshoe structures (Verma & Hemmati 2021). Quantitative analysis, which considered spanwise wavelength (λ_z) and periodicity of streamwise vortex pairs or ribs, established a clear connection to the elliptic-type

short-wavelength instability (Williamson 1996). In a recent study by Son *et al.* (2022), LEV instabilities were examined within the context of heaving oscillations that encompass both high aspect ratio wings and infinite-span foils. This study revealed changes in the strength of primary LEVs and TEVs in response to variations in St_c. These changes also coincided with alterations in the onset mechanisms of spanwise instability. The association of kinematics and spanwise instability was also observed across a range of chord-based St_c and ϕ (Verma & Hemmati 2023; Verma *et al.* 2023). In particular, Verma *et al.* (2023) discussed the growth of secondary hairpin-like structures and their association to the spanwise instability of rollers for different regimes of oscillating foil kinematics. This study also confirmed that the onset of three-dimensionality, in the form of secondary hairpin-like growth, is governed not only by changes in St_c, but also by ϕ. In particular, the interaction between primary and secondary LEVs can no longer govern the formation of secondary hairpin-like structures when ϕ increases from 90° to 270°, at $St_c = 0.32$. Rather, primary LEV–TEV interaction led to either their growth at $\phi = 180°$, or a complete absence at $\phi = 225°$ and 270°. Despite thorough investigations on the wake dynamics behind oscillating foils, there remains an unexplored fundamental mechanism that elucidates a direct transition from spanwise LEV instability to secondary hairpin-like structures in the wake of oscillating foils. Our objective is to gain a comprehensive understanding of this transition mechanism as the kinematics of oscillating foils undergoes changes in terms of St_c.

2. Problem description

The flow around an infinite-span (two-dimensional) foil with maximum thickness (D) to chord length (c) ratio $D/c = 0.1$ is examined numerically for a range of chord-based Strouhal numbers ($St_c = fc/U_\infty = 0.32$–$0.56$) and amplitude-based Strouhal numbers ($0.05 \leq St_A \leq 0.4$). Andersen *et al.* (2017) indicated that significant transitions in the wake of flapping foils were observable at $0.2 < St_A < 0.4$. This range also coincides with the optimal propulsive efficiency in swimming mammals (Triantafyllou *et al.* 2005; Smits 2019). The cross-section of the foil shown in figure 1 resembles a teardrop hydrofoil shape, which closely resembles the tailfin of a carangiform swimmer (Smits 2019) and was used in recent experimental investigations (Floryan *et al.* 2017; Van Buren, Floryan & Smits 2019). The Reynolds number is $Re = U_\infty c/\nu = 8000$, where U_∞ and ν represent the freestream velocity and kinematic viscosity of the fluid, respectively. This choice of Re agrees closely with the biological characteristics of some swimming fish (Anderson *et al.* 1998; Smits 2019; Verma & Hemmati 2021). Williamson (1996) mentioned that the shear layer transition regime lies at approximately $Re = 5300$, as also suggested by Zurman-Nasution *et al.* (2020). Since our Re corresponds to 8000, we are well past the transition regime. Further, Verma & Hemmati (2023) and Verma *et al.* (2023) reported a spanwise instability wavelength (λ_z) of approximately 1 at $Re = 8000$, which is close to the long-wavelength instability identified in purely pitching (Deng & Caulfield 2015) and heaving (Sun *et al.* 2018) foils at $Re = 1800$. Even at $Re = 20\,000$, Chiereghin *et al.* (2020) observed a similar wavelength of spanwise instability for the case of a plunging foil. Overall, the variation of Re within the range coinciding with biological swimming/flying might not offer a drastic change in the transition mechanism of spanwise instability discussed in our study.

The kinematics of the foil is prescribed by a coupled heaving and pitching motion, where the pitch axis is located at approximately $0.05c$ from the leading edge. Figure 1 marks the heave and pitch amplitudes as h_o and θ_o, respectively. The resultant trailing edge amplitude

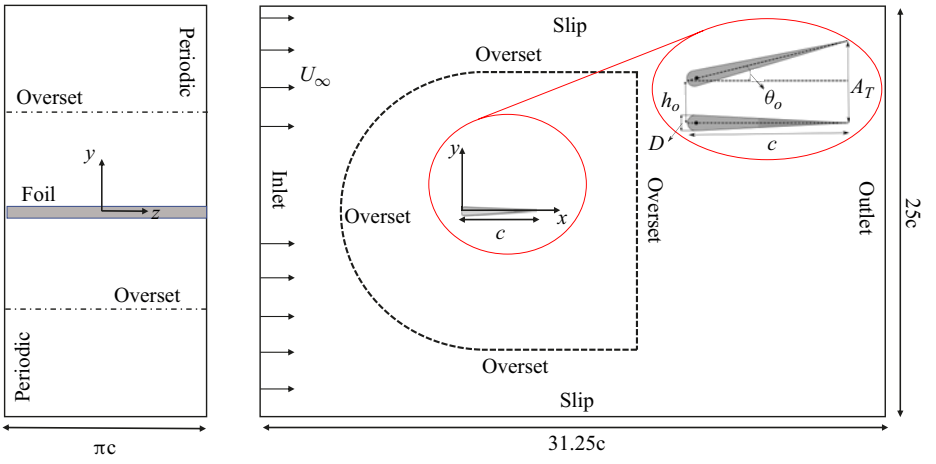

Figure 1. Schematic of the foil geometry and motion.

is also shown as A_T. The motion profiles of heave (h) and pitch (θ), where pitching has a phase advancement (or offset) ϕ relative to heaving, are represented as $h(t) = h_o \sin(2\pi ft)$ and $\theta(t) = \theta_o \sin(2\pi ft + \phi)$, respectively.

In order to present a broader association of secondary hairpin-like structures and kinematics of the foil, we also vary the phase offset (ϕ) between heaving and pitching motion in the range 90° to 270°. However, the discussion of results is focused at $\phi = 90°$, in order to explore and characterize the transition of spanwise instability of primary LEVs with increasing St_c. Verma & Hemmati (2023) and Verma *et al.* (2023) discussed findings at varying ϕ from 90° to 270°. The findings suggests that the origin of a secondary hairpin-like structure encounters changes at $St_c = 0.32$. The heave-dominated kinematics at $\phi = 90°$ is governed by an interaction between the primary and secondary LEVs over the foil boundary. However, at $\phi = 180°$, the interaction of primary LEV–TEV promoted a cooperative elliptic instability on the TEV, which subsequently transformed to a secondary hairpin-like structure. With further increase in ϕ to 225° and 270°, there was an absence of secondary hairpin-like generation. Later, Verma *et al.* (2023) also confirmed that with increasing St_c, the wake systems showed a dominant primary and secondary LEV interaction that contributes to the growth of secondary hairpin-like structures. However, a transition of primary LEV instability has not been discussed in detail. This appeared dominant only at $\phi = 90°$. Verma & Hemmati (2022*a*) further highlighted that the peak effective angle of attack (α_{eff}) is observed at $\phi = 90°$, which implies a correspondence to strong three-dimensionality in LEVs (Chiereghin *et al.* 2020). This substantiates our reasoning for depicting the results at $\phi = 90°$, so that a novel and vivid mechanism can be laid out to explain the transition of LEV spanwise instability to secondary hairpin-like structures. Figure 2(*a*) shows the variation of α_{eff} at $\phi = 90°$, while St_c increases from 0.32 to 0.56. Moreover, peak α_{eff} increases as St_c varies in this range. The peak magnitude coincides with $t^+ = 0.5$. Figure 2(*b*) provides a variation of α_{eff} at different ϕ in the range $90° \leq \phi \leq 270°$ for the case $St_c = 0.32$. The peak α_{eff} coincides with $\phi = 90°$, which decreases with increasing ϕ towards 270°. The observations are consistent with discussion presented by Verma & Hemmati (2022*a*), where the variation also demonstrates a transition of kinematics from heave domination to an onset of pitch

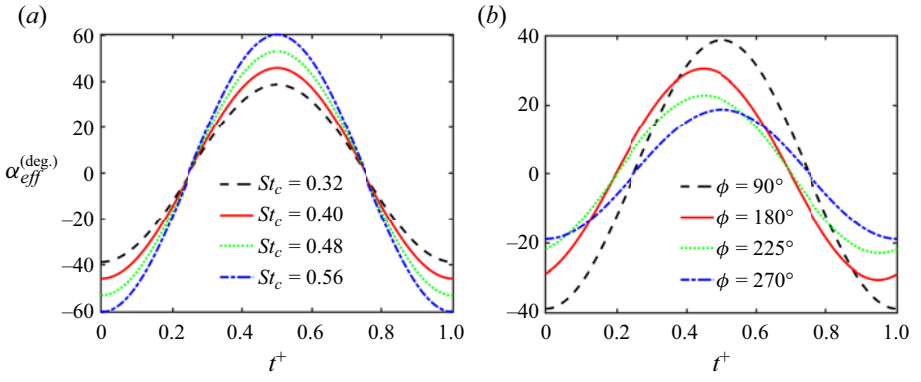

Figure 2. Variation of α_{eff} within one oscillation period at (*a*) increasing St_c and $\phi = 90°$, and (*b*) increasing ϕ and $St_c = 0.32$.

domination. The greater α_{eff} observed at $\phi = 90°$ supports the discussion that the LEV three-dimensionality is expected to be the strongest within the range considered here.

2.1. *Computational method*

The continuity and Navier–Stokes equations are solved directly using OpenFOAM, which is a numerical package based on the finite-volume method. This platform is used extensively for simulating wake dynamics behind oscillating foils and panels (Senturk & Smits 2019; Verma & Hemmati 2021, 2022*b*; Verma, Freeman & Hemmati 2022). The kinematics of the oscillatory foil is modelled using the overset grid assembly method, based on a stationary background grid and a moving overset grid that are merged for the simulation (Petra 2019). More details of the method can be found in Verma & Hemmati (2020, 2021, 2022*a*).

The computational domain and grid are presented in figures 1 and 3, respectively, highlighting the C-type overset boundary that houses the foil. The boundary conditions at the inlet are prescribed a uniform fixed velocity (Dirichlet) and a zero normal gradient (Neumann) for pressure. At the outlet, a zero-gradient outflow boundary condition is implied (Deng & Caulfield 2015). The top and bottom walls are further prescribed a slip boundary condition that effectively models open-channel or free-surface flows, and closely resemble the experimental and computational conditions of Van Buren *et al.* (2019) and Hemmati, Van Buren & Smits (2019), respectively. At the boundary of the foil, a no-slip condition for velocity and a zero-gradient condition for pressure are ensured. The periodic boundary condition is further implemented on the side boundaries, coinciding with the spanwise extent of the foil. It provides an effective way to model flows over bodies with infinite spans without the end or tip effects.

A grid independence analysis is completed at $Re = 8000$, $h_o/c = 0.25$, $\theta_o = 15°$, $\phi = 270°$ and $St_c = 0.67$. This enables comparative evaluation of the numerical results with respect to experiments of Van Buren *et al.* (2019). Table 1 summarizes the grid convergence results involving three grids: Grid1 (coarse mesh), Grid2 (fine mesh) and Grid3 (very fine mesh). The ratio (δ^*) of minimum grid size element (Δx) to Kolmogorov scale (η) is kept approximately below 10, within the critical region near the foil ($x < 2.5c$), specifically for Grid2 and Grid3 (see table 1). This region corresponds to the origin of spanwise instability and secondary hairpin-like structures that emerge and grow in the wake (Verma & Hemmati 2021, 2023). The relative error in prediction of $\overline{C_T}$

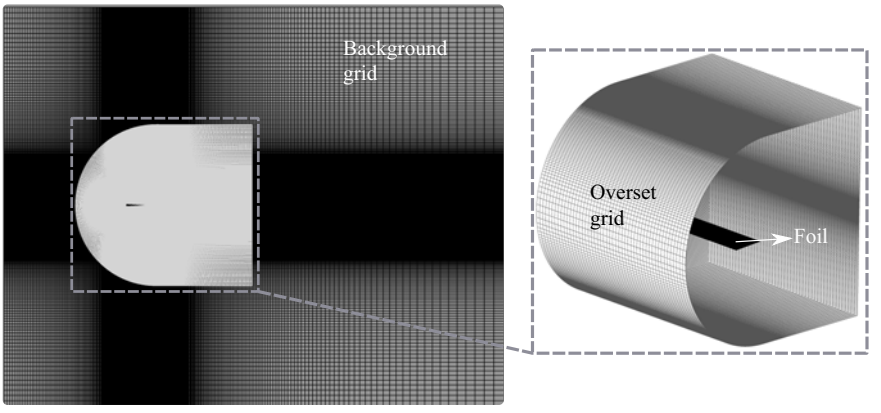

Figure 3. Depiction of three-dimensional background and overset grids.

Study	N_{total}	$\overline{C_T}$	C_L^{rms}	ϵ_T	ϵ_L^{rms}	$x =$	$1c$	$2.5c$	$5c$
Grid1	8.4×10^6	0.64	2.86	0.084	0.010	$\delta^* =$	7.3	16.9	55.2
Grid2	1.7×10^7	0.60	2.84	0.017	0.003	$\delta^* =$	3.7	8.5	15.8
Grid3	3.1×10^7	0.59	2.83	0.001	—	$\delta^* =$	1.8	4.2	7.9
Exp.	—	0.59	—	—	—	$\delta^* =$	—	—	—

Table 1. Grid refinement details for the current study, where N_{total} represents the sum of hexahedral elements in the background grid and overset grid.

($\epsilon_T = |\overline{C_{T,exp}} - \overline{C_T}|/\overline{C_{T,exp}}$), calculated with respect to the experimental results of Van Buren *et al.* (2019), is below 5 % for Grid2. Similarly, $\epsilon_L^{rms} (= |C_{L,Grid3}^{rms} - C_L^{rms}|/C_{L,Grid3}^{rms})$, calculated with respect to the finest grid (Grid3), is below 0.1 %. This agreement in results provides sufficient confidence in Grid2 for our analysis. Details for verification and validation of the numerical solver, with respect to the domain size, spatial and temporal grid, overset grid assembly solver and boundary conditions, can be found in Hemmati *et al.* (2019) and Verma & Hemmati (2020, 2021, 2023).

3. Results and discussion

Mechanisms responsible for the onset of secondary hairpin-like vortex growth are discussed qualitatively at $\phi = 90^\circ$ with increasing St_c from 0.32 to 0.56. Here, 'secondary' refers to any system of coherent structure that is characterized by a significant portion of its vorticity oriented in the streamwise direction. This terminology has been used in various studies concerned with oscillating wings (Visbal 2012; Zhang & Huang 2023). For instance, Visbal (2012) observed and reported the existence of secondary filaments as the LEV disintegrated at high oscillation frequency of a plunging wing. Zhang & Huang (2023) recently characterized straining and stretching of secondary filaments that evolve into one-legged hairpin-like vortices on the surface of a batoid fish. These filaments also showcased a significant streamwise vorticity component. Horseshoe and hairpin structures have been widely explained as coherent vortical structures observed in turbulent boundary layers and bluff-body wakes (Mittal & Balachandar 1995; Williamson 1996). In general, Smith *et al.* (1991) commented that such structures characterize legs that possess

a symmetry in the streamwise vorticity. However, in many cases, existence of multiple hairpin structures in localized spatial regions leads to loss in the symmetry of legs. Thus Smith *et al.* (1991) extended this description to explain asymmetric hairpins, which are also referred as quasi-streamwise vortices. One such example resembles a one-legged hairpin structure reported by Smith *et al.* (1991) whose head possesses a significant spanwise component of vorticity, while only a single leg develops and extends in the wake. Here, we also differentiate the hairpin structures (symmetric) from 'hairpin-like' structures. There exists substantial qualitative evidence to confirm that hairpins identified in our study do not necessarily characterize a symmetric growth of hairpin legs.

A brief summary of the results presented by Verma & Hemmati (2022*a*) at $St_c = 0.32$ is provided here for comparison, and to establish the basis of our analysis at higher St_c. The spatio-temporal wake evolution at increasing St_c is demonstrated using isosurfaces of Q-criterion, $Q^+ = Qc^2/U_\infty^2$, which identify primary LEV rollers and secondary hairpin-like structures that dominate the wake. The evolution of spanwise undulations on the primary LEV, and its contribution towards secondary hairpin-like structures, is further explored at higher St_c in later subsections. This particularly highlights the existence of a unique transition mechanism for spanwise LEV instability. This transition is characterized by a supplemental growth of secondary hairpin-like structures in the wake of oscillating foils.

3.1. *Primary LEV instability and single hairpin-like system at* $St_c = 0.32$

Growth of a secondary LEV roller leads to an elliptic-type instability (Leweke & Williamson 1998) of counter-rotating primary and secondary LEVs (Verma & Hemmati 2023; Verma *et al.* 2023). The elliptic instability wavelength ($\lambda_z^+ = \lambda_z/c$) is estimated by following the procedure discussed in Verma & Hemmati (2021, 2023). These estimates reveal $\lambda_z^+ = 0.86$, which also agrees with the instability wavelengths reported by Verma & Hemmati (2021, 2023). Chiereghin *et al.* (2020) also obtained a similar estimate of the spanwise instability observed on an isolated LEV structure. Son *et al.* (2022) further suggested that despite slight changes in the estimates of λ_z^+ with varying kinematics of a plunging foil, the wavelength remains of the order of the foil's chord. Figures 4(*a*) and 4(*b*) depict the wake at $t^+ = 0.5$ and 0.75, respectively. Here, t^+ represents the non-dimensional time scale in terms of oscillation cycle time (T), i.e. $t^+ = t/T$. The instantaneous variation of α_{eff} within a single oscillation period is also shown to depict the association of growing secondary hairpin-like structures over the foil boundary, and the attainment of peak α_{eff}. Streamwise vorticity filaments emanate from the secondary LEV and initially arrange in the spanwise configuration of nascent hairpin-like vortices (Verma & Hemmati 2023). This can be visualized in figure 4(*a*). Under the influence of imposed strain fields and stretching from the neighbouring primary LEV, legs of the hairpin-like structures extend as the LEV roller shed in the wake, which ultimately leads to the formation of rib pairs (R1′) downstream of the foil trailing edge. Moving our attention to the primary LEV ($\mathrm{LEV1}_{ac}$ or $\mathrm{LEV1}'_{ac}$ from the previous oscillation cycle), figures 4(*a*) and 4(*b*) demonstrate its simultaneous advection with other shed TEVs and secondary hairpin-like vortex structures and ribs (R1′). This $\mathrm{LEV1}_{ac}$ experiences a higher amplitude undulation just ahead of its separation, while hairpin-like vortex legs grow and form rib pairs (see figure 4*b*). Rib pairs R1′ demonstrate this configuration based on the wake evolution in the previous oscillation cycle. Also, the $\mathrm{TEV1}_c$ marked in figure 4(*b*) is in its nascent stages of growth. As $\mathrm{LEV1}_{ac}$ further advects downstream, it does not show any

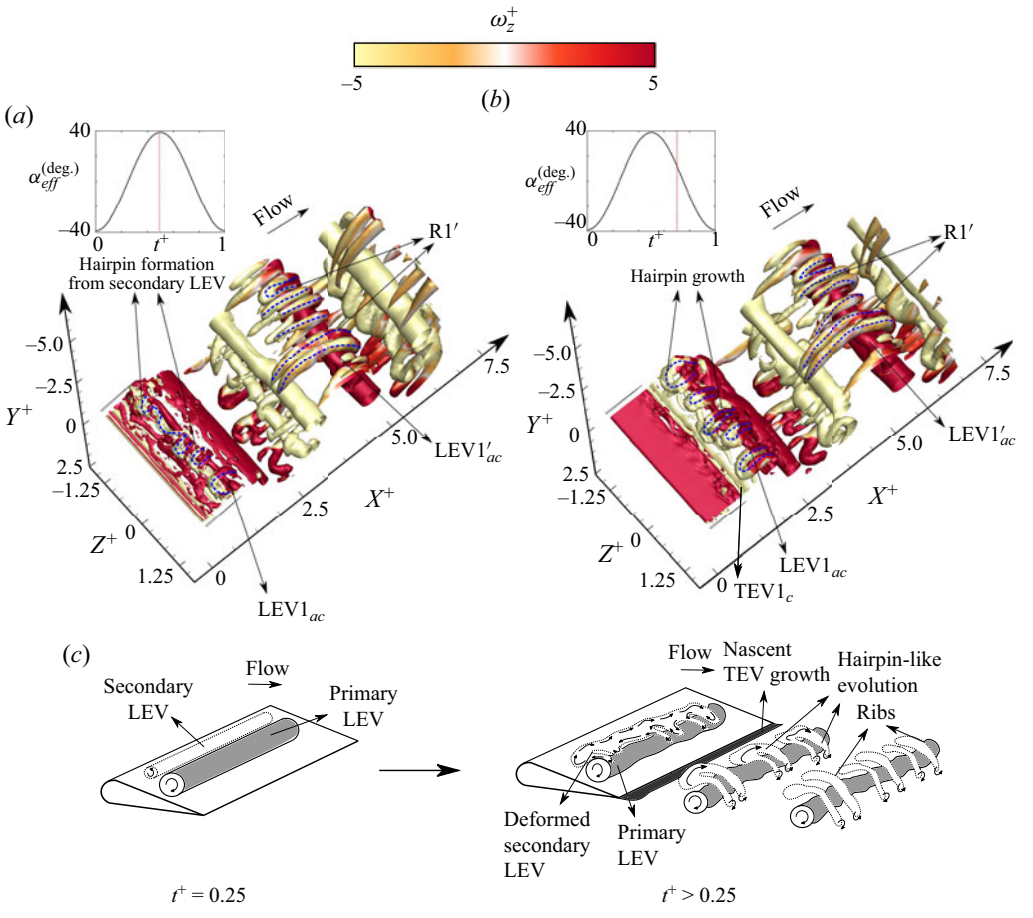

Figure 4. Wake evolution at $\phi = 90^\circ$ and $St_c = 0.32$. The time instants correspond to (*a*) $t^+ = 0.5$ and (*b*) $t^+ = 0.75$. Each stage is represented using isosurfaces of $Q^+ (= Qc^2/U_\infty^2) = 0.032$, which are coloured based on $|\omega_z^+| = 5$. (*c*) Vortex skeleton model depicting the changes in wake topology and growth of secondary hairpin-like structures at $St_c = 0.32$.

substantial increase in its undulation amplitude (see figure 4*b*). No prominent bending of LEV1′$_{ac}$ is apparent at $X^+ > 5$, despite consistent elongation of rib pairs. Therefore, the only contribution to the growth of secondary hairpin-like structures is attributed to the streamwise vorticity outflux from the secondary LEV roller, described recently by Verma & Hemmati (2023) and Verma *et al.* (2023). A vortex skeleton model is presented in figure 4(*c*), which summarizes the wake evolution and growth of secondary hairpin-like structures at $St_c = 0.32$.

3.2. *Transition of primary LEV instability to a secondary hairpin-like vortex system*

A supplemental hairpin-like system is identified at increasing St_c beyond 0.32. Figures 5(*a*) and 5(*b*) depict the evolution of primary LEV2$_{ac}$ at $St_c = 0.40$, along with the growth of secondary hairpin-like filaments near the foil trailing edge. The onset of these hairpin-like vortex filaments follows a mechanism similar to that outlined before for $St_c = 0.32$ (Verma & Hemmati 2023; Verma, Khalid & Hemmati 2024). The λ_z^+ value for the primary LEV during its presence over the foil is estimated to be 0.43. This is similar to the instability

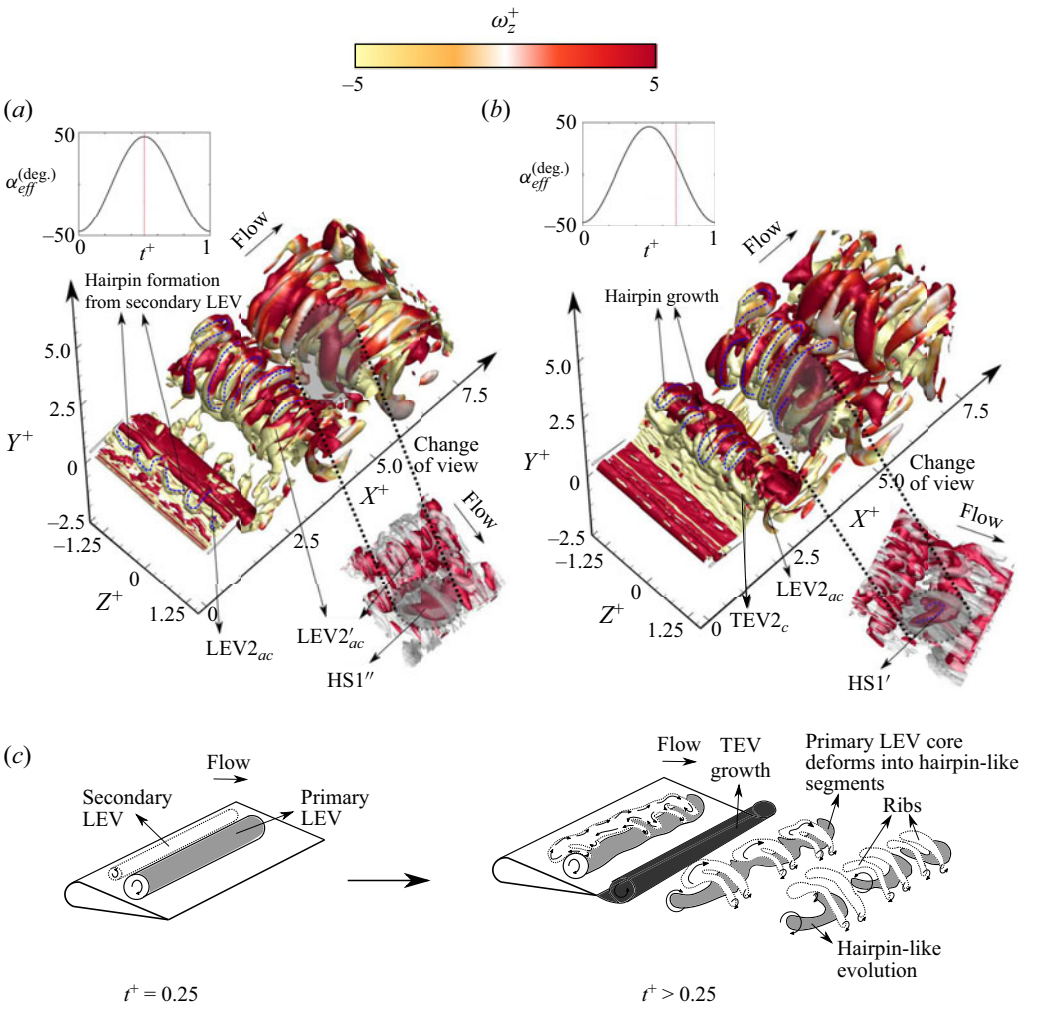

Figure 5. Wake evolution at $\phi = 90^\circ$ and $St_c = 0.40$. The time instants correspond to (*a*) $t^+ = 0.5$ and (*b*) $t^+ = 0.75$. Each stage is represented using isosurfaces of $Q^+ = 0.032$, which are coloured based on $|\omega_z^+| = 5$. The change in orientation provides enhanced visualization of secondary hairpin-like vortex structures represented by the highlighted regions in dark grey. Note that the pre-existing hairpin-like structures have been displayed with reduced opacity (light grey). (*c*) Vortex skeleton model depicting the changes in wake topology and growth of secondary hairpin-like structures at $St_c = 0.40$.

wavelength predicted by Sun *et al.* (2018) for mode S ($\lambda_z^+ = 0.393$) in the wake of a heaving foil. At $t^+ = 0.5$, LEV2$_{ac}$ (see figure 5*b*) shows a relatively larger bending amplitude compared to LEV1$_{ac}$ at $St_c = 0.32$ (see figure 4*b*). This also coincides with a TEV growth (see TEV2$_c$ in figure 5*b*) and consistent elongation of hairpin-like legs to form rib pairs in the wake. To further detail the behaviour of LEV2$_{ac}$ downstream, figures 5(*a*) and 5(*b*) highlight the growth of dominant secondary hairpin-like like vortex structures (HS1″ and HS1′) along the spanwise direction at $X^+ > 2.5$. Growth of these structures qualitatively appears on account of the strong bending and dislocations on the primary LEVs (e.g. LEV2′$_{ac}$). This closely resembles the observations of Mittal & Balachandar (1995) in the wake of a stationary circular cylinder highlighting the

mechanism for horseshoe-like formations in terms of vortex core instability (Brede *et al.* 1996; Williamson 1996). Ryan, Butler & Sheard (2012) also presented vivid observations on counter-rotating vortex pairs, where the stronger vortex exhibits spanwise dislocations that were triggered by existing rib structures. The rib pairs are also noted in figures 5(*a*) and 5(*b*), which evolve in conjunction with secondary hairpin-like structures (HS1′ and HS1″). More elaborate discussion and evidence for this mechanism will be provided in the next subsection.

Although results in figure 5 are limited to $X^+ = 7.5$, long-term evolution of the secondary hairpin-like structures will follow the mechanism that contributes to rib formation, as suggested by Mittal & Balachandar (1995). The legs of a secondary hairpin-like vortex will elongate and resemble an intermediate hairpin-like configuration. The head of this structure could then bifurcate, and thus form a supplemental rib system in the wake (Mittal & Balachandar 1995; Williamson 1996). In comparison to $St_c = 0.32$, it is clear that enhanced deformation and bending of the primary LEV at $St_c = 0.40$ leads to the growth of a dominant secondary hairpin-like configuration ahead of $X^+ = 5$. A vortex skeleton model is presented in figure 5(*c*), which summarizes the wake evolution and growth of secondary hairpin-like structures at $St_c = 0.40$.

The evolution of the wake at $St_c = 0.48$ and 0.56 is shown in figures 6(*a–d*). The onset of secondary hairpin-like growth near the foil trailing edge, and LEV instability, remains prominent. The estimated λ_z^+ for the primary LEV is 0.43, which is also similar to the instability wavelength reported at $St_c = 0.40$. However, the legs of the hairpin-like vortices are more elongated (see figures 6*a*,*d*) at the instance of shedding, compared to $St_c = 0.32$ and 0.40. We also note that growth of the TEV structure is accelerated at $St_c = 0.48$ and 0.56 (see $\mathrm{TEV3}_c$ and $\mathrm{TEV4}_c$ in figures 6*b*,*d*), compared to the structures in wakes observed at $St_c = 0.32$ and 0.40, respectively. Bending of separated $\mathrm{LEV3}_{ac}$ is imminent at $St_c = 0.48$ in figure 6(*a*). The maximum bending amplitude is approximately at the mid-span ($Z^+ = 0$), with two identical arches forming at the neighbouring ends of the centre arch. As $\mathrm{LEV3}_{ac}$ evolves downstream, dual hairpin-like structures become evident, i.e. HS2 in figure 6(*b*). These emerge on account of the eventual amplification of the arch amplitude, which was initially observed on $\mathrm{LEV3}_{ac}$ in figure 6(*a*). Compared to HS1′ and HS1″ observed at $St_c = 0.40$, the legs of HS2 undergo a relatively faster elongation at $St_c = 0.48$, and consequently wrap around the shed $\mathrm{TEV3}_c$ roller in figure 6(*b*). A consequence of this process is an early transition to another hairpin-like vortex, which then tears around its head to form ribs. The pair of ribs that originates from the primary LEV ($\mathrm{R4}'_2$ in figure 6*b*) approximately maintains its vorticity magnitude and size until a higher streamwise distance, compared to the pairs (marked as $\mathrm{R4}'_1$) that originate from the hairpin-like evolution associated with the vorticity outflux from the secondary LEV over the foil boundary. Such stronger and weaker rib pairs coexist in the wake, while originating through different evolution mechanisms.

The presence of secondary hairpin-like vortex structures that originate from deforming LEV in the wake is consistently observed at $St_c = 0.56$ in figures 6(*c*) and 6(*d*). Two dominant hairpin-like structures (HS3′) are identified and marked in figure 6(*c*), which evolve via bending of the previously shed LEVs from the bottom side of the foil. A similar bending and transition to a dual hairpin-like system is again evident for $\mathrm{LEV4}_{ac}$ (shed from the foil top) in figure 6(*d*), which are marked as HS3. Elongated legs of hairpin-like structures formed on account of the vorticity outflux from the secondary LEV are identified as R5 (see figure 6*c*), since they eventually extend to form rib pairs downstream ($\mathrm{R6}'_1$ in figure 6*d*). Later, HS3 tears up from its head and forms a

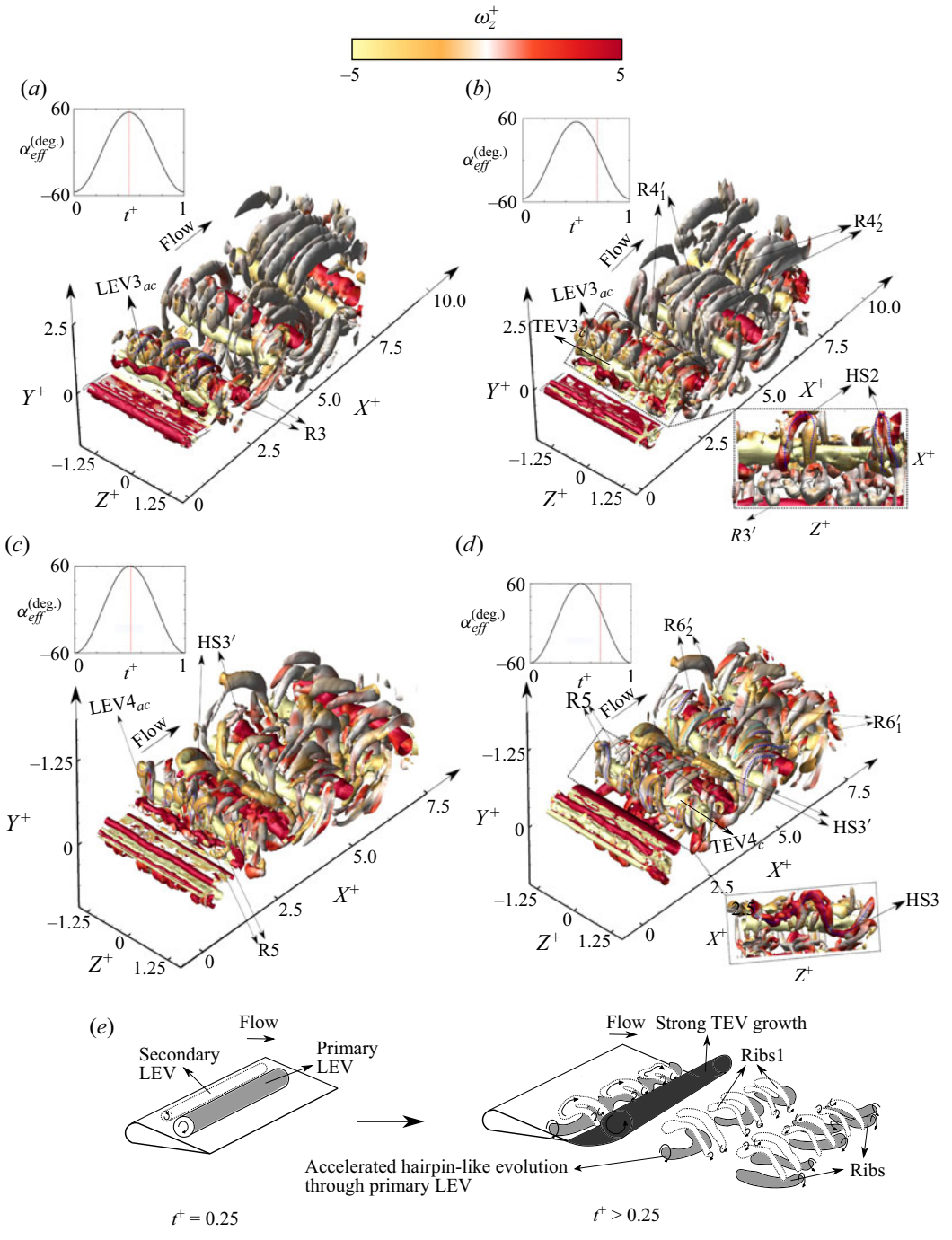

Figure 6. Wake evolution at $\phi = 90^\circ$ and (*a*,*b*) $St_c = 0.48$, (*c*,*d*) $St_c = 0.56$. The time instants correspond to (*a*,*c*) $t^+ = 0.5$ and (*b*,*d*) $t^+ = 0.75$. Each stage is represented using isosurfaces of $Q^+ = 0.032$, which are coloured based on $|\omega_z^+| = 5$. (*e*) Vortex skeleton model depicting the changes in wake topology and growth of secondary hairpin-like structures at $St_c = 0.48$ and 0.56.

supplementary system of paired rib structures downstream. These are labelled $R6'_2$ in figure 6(*d*), which elongate through the HS3′ system of secondary hairpin-like structures (see figure 6*c*). Overall, the wake dynamics closely resembles observations at $St_c = 0.48$, where the presence of secondary hairpin-like structures in the wake is uniquely attributed to two separate mechanisms. It is also interesting to note that bending of the primary LEV and formation of the resulting hairpin-like structure is accelerated at $St_c > 0.40$. For example, legs of the hairpin-like structures at $St_c = 0.48$ and 0.56 are highly elongated around $X^+ = 2.5$, while these structures still lack elongation by $X^+ = 5$ at $St_c = 0.40$ (see figure 5*b*). Furthermore, wake systems visualized at $St_c > 0.40$ feature secondary hairpin-like structures that originate from the primary LEV, and those evolving from the secondary LEV near the foil trailing edge become coherent at a shorter streamwise distance from the foil trailing edge compared to $St_c = 0.32$. A vortex skeleton model is presented in figure 6(*e*), which highlights the wake evolution and growth of secondary hairpin-like structures at $St_c = 0.48$ and 0.56.

To summarize and better explain the implications of increasing St_c, figure 7 describes a combined wake model that highlights the transition process and growth of secondary hairpin-like structures. At approximately $t^+ = 0.25$, a secondary LEV remains persistent for the entire St_c range under consideration. This LEV forms a counter-rotating vortex pair of unequal strength with the primary LEV. At $St_c = 0.32$, the primary LEV does not undergo any substantial deformation, while the legs of hairpin-like structures elongate and evolve on account of the braid vorticity straining (Mittal & Balachandar 1995; Williamson 1996). These then transform to counter-rotating rib pairs. With increasing St_c (i.e. $St_c > 0.32$), the primary LEV core begins a higher-amplitude undulation, compared to those observed at $St_c = 0.32$. At higher St_c (i.e. $St_c = 0.48$ and 0.56), the formation process of hairpin-like structures originating from the primary LEV accelerates, where they gain coherence at a relatively shorter distance from the trailing edge compared to the lower St_c cases. This also coincides with a faster TEV growth as St_c increases from 0.32 to 0.56. An early amplification of the undulating arches of the primary LEV could be associated with an early segmentation and transformation to hairpin-like structures. This will be confirmed quantitatively in the next subsection. Subsequently, continuous straining of the existing secondary hairpin-like vortex pairs and braid vorticity will promote the transition of newly formed hairpin-like structures from the primary LEV, to additional rib pairs (marked as Ribs2 in figure 7). We now present and discuss detailed physical reasoning behind observations presented in this section.

3.3. *Mechanism for spanwise instability transition*

Presented results suggest that the primary LEV undergoes high-amplitude undulation at $St_c > 0.32$, which leads to the formation of secondary hairpin-like structures in the wake. However, we need more detailed analysis of the flow to better understand the physical mechanism attributed to this phenomenon. To this end, we first focus on the principles of vortex stretching/compression term of the vorticity budget (Wu, Ma & Zhou 2006). This term is represented as $\langle \Omega_x \rangle \langle S_{xx} \rangle$, where $\langle \Omega_x \rangle$ and $\langle S_{xx} \rangle$ are time-averaged vorticity and rate of strain in the streamwise direction. Based on the positive or negative sign of this quantity, it can be interpreted as vortex stretching or compression, respectively (Bilbao-Ludena & Papadakis 2023).

Figures 8(*a*) and 8(*b*) provide an instantaneous snapshot of the wake at $St_c = 0.32$, as $LEV1_{ac}$ sheds from the trailing edge. We also observe $TEV1_c$ to grow from the bottom side of the foil. It is important to note that the value of the Q-criterion is adjusted

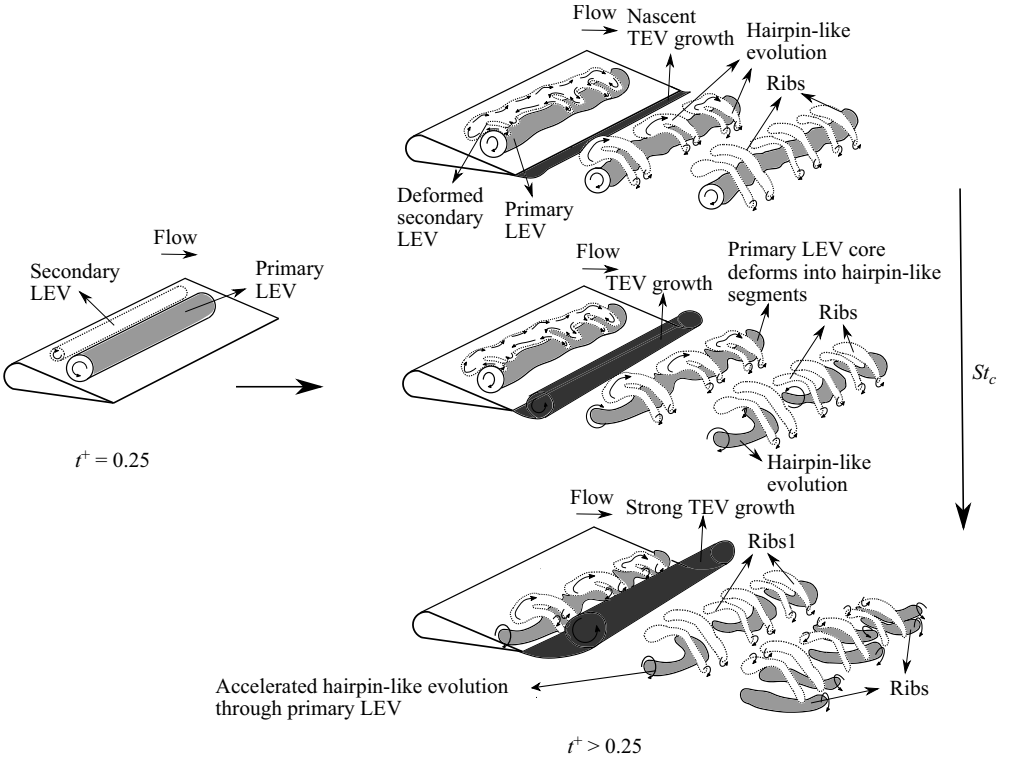

Figure 7. Vortex skeleton model depicting the changes in wake topology with increase in St_c.

relative to figures 4(*a*) and 4(*b*) to emphasize evolution of the spanwise instability of the primary rollers (i.e. LEVs and TEVs). The spanwise dislocations on LEV1$_{ac}$ are evident, although they fail to transition towards any secondary hairpin-like system in the wake. Figures 4(*a*) and 4(*b*) have already confirmed that the wake is only dominated by hairpin-like vortex structures that evolve from deforming a secondary LEV. Contrary to the observations at $St_c = 0.32$, figures 8(*c*) and 8(*d*) qualitatively confirm that the primary LEV2$_{ac}$ identified at $St_c = 0.40$ undergoes large-amplitude undulations that later promote vortex tearing. The spanwise locations where the tearing occurs are marked in figure 8(*b*). The subsequent straining from pre-existing hairpin-like structures and developing TEV2$_c$ eventually transforms the undulated LEV2$_{ac}$ to a hairpin-like system identified earlier, in figure 5. The process of primary LEV evolution remains consistent at $St_c = 0.48$ and 0.56. For brevity, only the wake corresponding to $St_c = 0.48$ is shown in figures 8(*e*) and 8(*f*). The primary leading (LEV3$_{ac}$) and trailing (TEV3$_c$) edge rollers are marked, while the enlargement of bending undulations is evident on LEV3$_{ac}$ in figure 8(*f*). The tearing of LEV3$_{ac}$ eventually occurs at localized locations, similar to LEV2$_{ac}$ at $St_c = 0.40$, which then promotes growth of a hairpin-like vortex system identified in figure 6. Overall, the transition in primary LEV instability is apparent beyond $St_c = 0.32$.

Distribution of the mean vortex stretching/compression is now evaluated on 'focus planes' marked in figures 8(*a–f*) along the span of the primary LEV in figure 9. These represent localized regions around dislocations of relatively larger spatial scales, since they are more susceptible to concentrated strain rates and vortex tearing (Ryan *et al.* 2012). For $St_c = 0.32$, the planes are represented at spanwise locations corresponding to

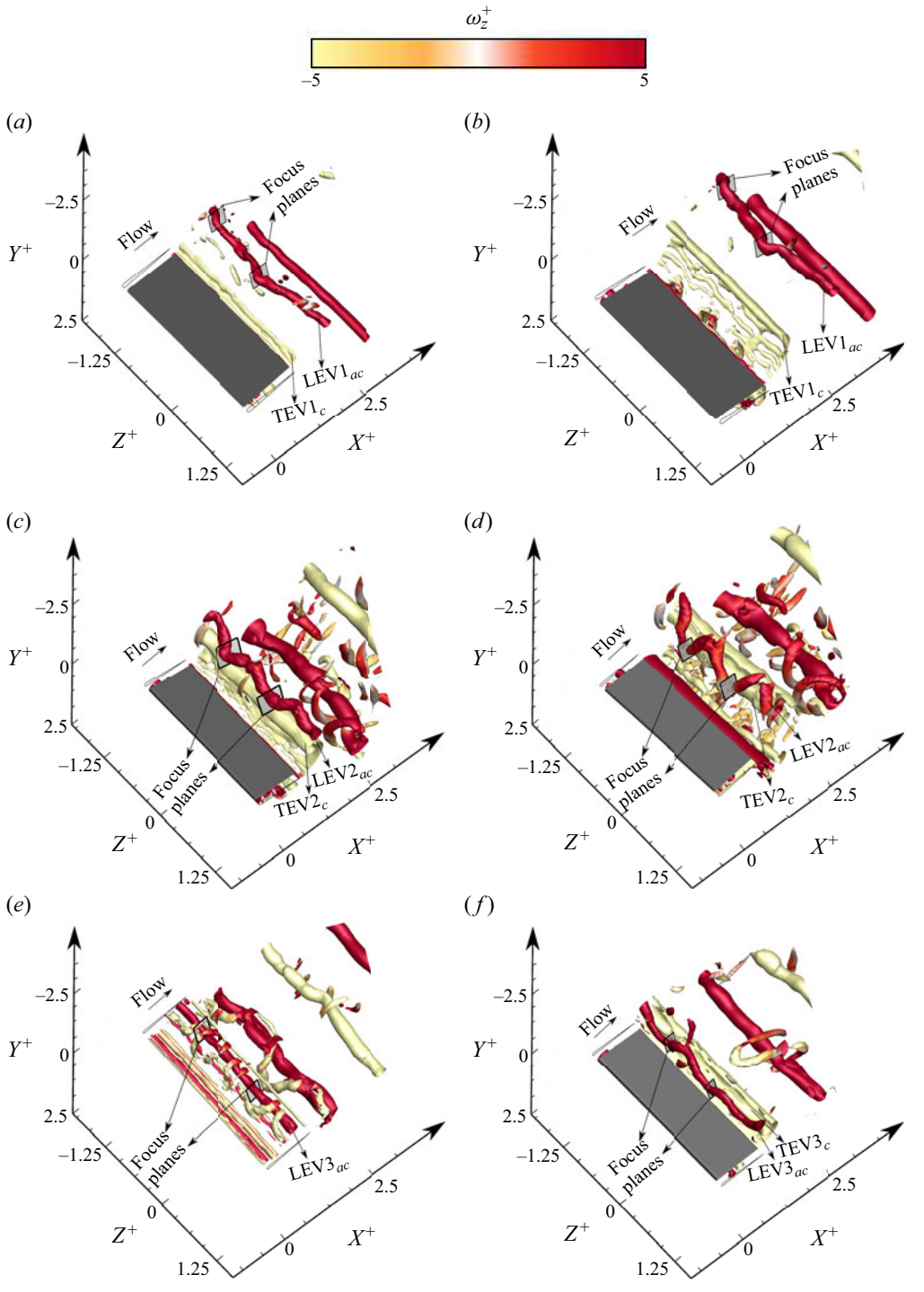

Figure 8. Wake evolution at $\phi = 90^\circ$ and (*a*,*b*) $St_c = 0.32$, (*c*,*d*) $St_c = 0.40$ and (*e*,*f*) $St_c = 0.48$. The time instants are (*a*,*c*,*e*) $t^+ = 0.5$ and (*b*,*d*,*f*) $t^+ = 0.75$. Each stage is represented using isosurfaces of $Q^+ = 9.6$, which are coloured based on $|\omega_z^+| = 5$.

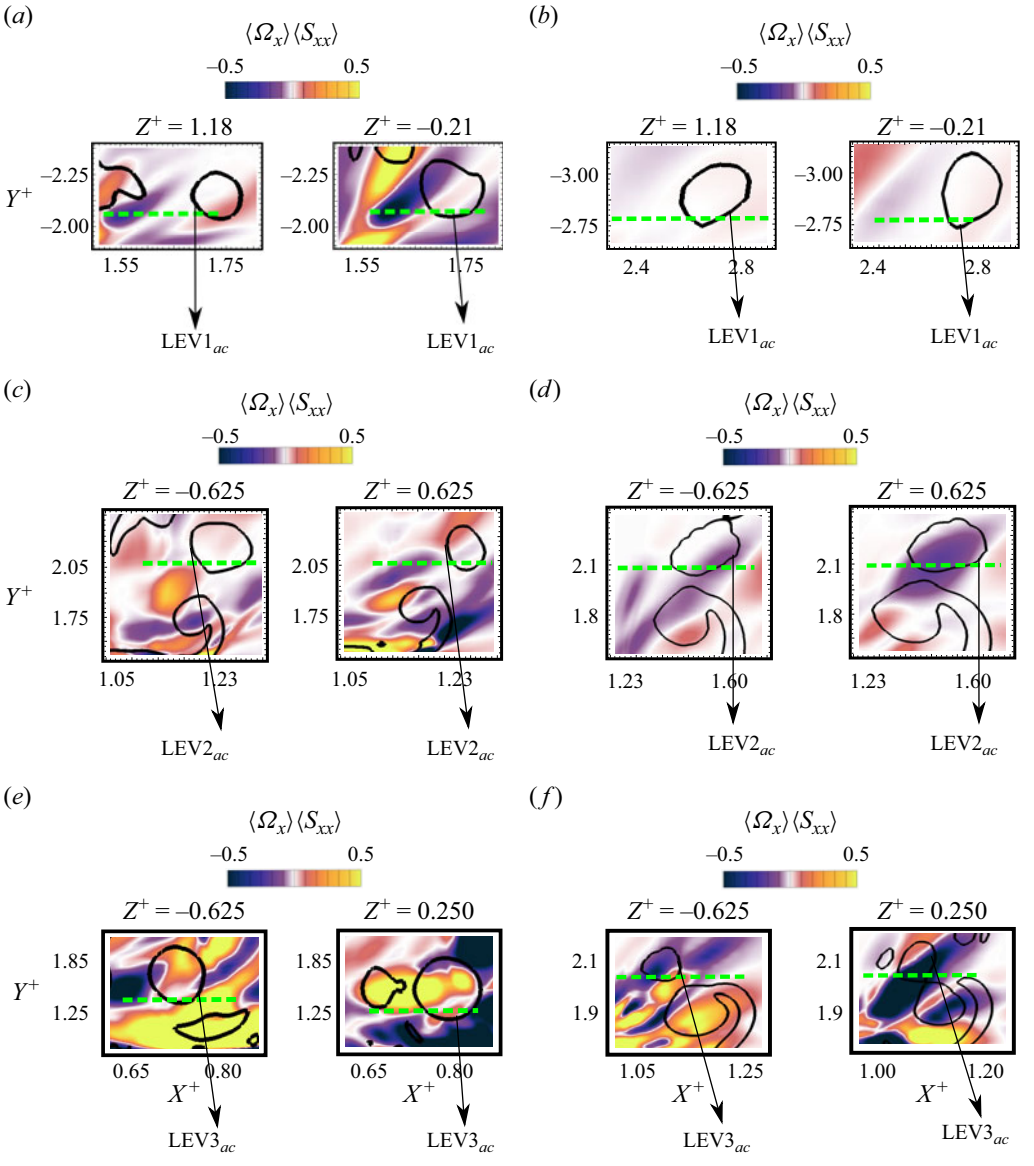

Figure 9. Distribution of vortex compression ($\langle\Omega_x\rangle\langle S_{xx}\rangle$) for (*a*,*b*) $St_c = 0.32$, (*c*,*d*) $St_c = 0.40$ and (*e*,*f*) $St_c = 0.48$. The locations of *XY*-planes correspond to spanwise dislocations on the primary LEV. The planes are identified visually in figures 8(*a–f*). The time instants are (*a*,*c*,*e*) $t^+ = 0.5$ and (*b*,*d*,*f*) $t^+ = 0.75$. Black solid lines on the planes represent primary LEV and TEV rollers identified using the *Q*-criterion ($Q^+ = 9.6$).

$Z^+ = -0.21$ and 1.18. It is evident that the neighbouring regions around the primary LEV core at $t^+ = 0.5$ in figure 9(*a*) exhibit localized axial vortex compression on account of negative $\langle\Omega_x\rangle\langle S_{xx}\rangle$. However, the magnitude of compression reduces at both spanwise locations as the primary LEV1$_{ac}$ advects downstream in the wake at $t^+ = 0.75$ (see figure 9*b*). These observations are also confirmed quantitatively in figures 10(*a*) and 10(*b*), which correspond to spanwise locations $Z^+ = -0.21$ and 1.18, respectively. The profiles of $\langle\Omega_x\rangle\langle S_{xx}\rangle$ are extracted along the streamwise direction, represented by the green dashed

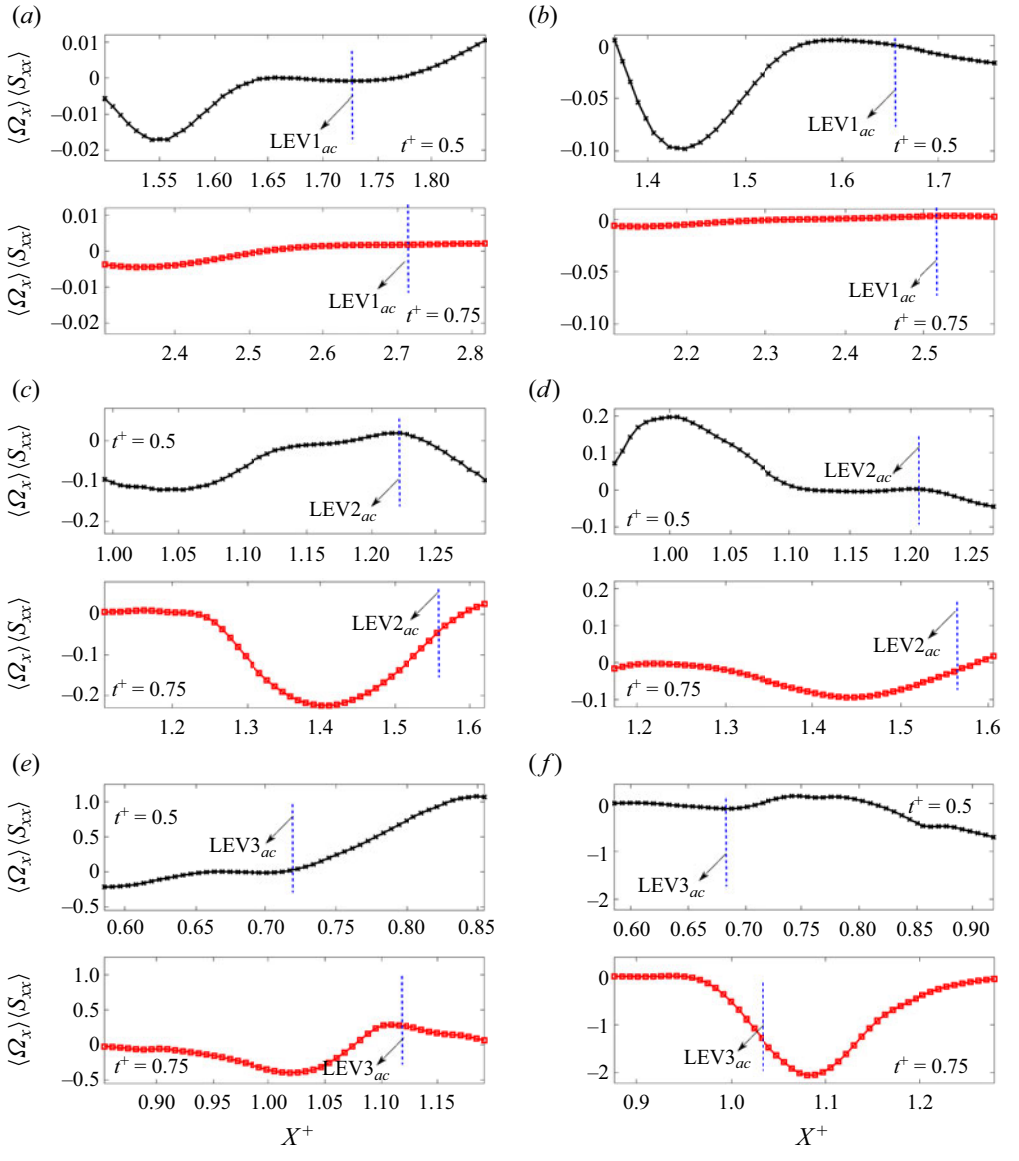

Figure 10. Quantitative distribution of $\langle\Omega_x\rangle\langle S_{xx}\rangle$ at (*a*,*b*) $St_c = 0.32$, (*c*,*d*) $St_c = 0.40$ and (*e*,*f*) $St_c = 0.48$. The extracted data on *XY*-planes shown in figures 9(*a–f*), correspond to the green dashed lines marked in contours of $\langle\Omega_x\rangle\langle S_{xx}\rangle$.

line on the slices shown in figures 9(*a*) and 9(*b*). The location of the line is determined based on where the primary LEV bending emerges, and amplifies, as it advects in the wake. The temporal decrease in magnitude of vortex compression is consistent at both spanwise locations. Particularly at $Z^+ = -0.21$ (see figure 10*a*), the peak in magnitude of $\langle\Omega_x\rangle\langle S_{xx}\rangle$ at $t^+ = 0.75$ decreases from 0.02 (at $t^+ = 0.5$) to approximately 0.004 in regions upstream of the dominant spatial dislocation identified on LEV1$_{ac}$. Similarly, at $Z^+ = 1.18$ (see figure 10*b*), the peak in magnitude of $\langle\Omega_x\rangle\langle S_{xx}\rangle$ at $t^+ = 0.75$ decreases from 0.1 (at $t^+ = 0.5$) to approximately 0.0055.

Figures 9(*c*) and 9(*d*) demonstrate the distribution of $\langle \Omega_x \rangle \langle S_{xx} \rangle$ at 'focus planes' marked in the wake at $St_c = 0.40$ (see figures 8*c*,*d*). The spanwise locations along the primary LEV2$_{ac}$ correspond to $Z^+ = -0.625$ and 0.625, respectively. The distribution now depicts contrasting aspects compared to discussion presented with respect to figures 9(*a*) and 9(*b*) at $St_c = 0.32$. We witness an increased compression magnitude at $t^+ = 0.75$ compared to $t^+ = 0.5$, at both spanwise locations. The quantitative profiles extracted in the streamwise direction at $Z^+ = -0.625$ and 0.625 are shown in figures 10(*c*) and 10(*d*), respectively. These confirm that an enhanced vortex compression becomes apparent as LEV2$_{ac}$ advects downstream. At $Z^+ = -0.625$ (see figure 10*c*), the peak magnitude of $\langle \Omega_x \rangle \langle S_{xx} \rangle$ at $t^+ = 0.75$ increases from 0.125 (at $t^+ = 0.5$) to approximately 0.23, while at $Z^+ = 0.625$ (see figure 10*d*), it increases from a near-zero value (at $t^+ = 0.5$) to approximately 0.1 at $t^+ = 0.75$. Note that the positive value of $\langle \Omega_x \rangle \langle S_{xx} \rangle$ upstream of LEV2$_{ac}$ at $t^+ = 0.5$, on $Z^+ = 0.625$ (figure 10*d*), denotes axial stretching instead of compression. The source of magnified compression observed at both Z^+ locations is associated with the growth of TEV2$_c$ that occurs in the close proximity of the primary LEV2$_{ac}$ (see figures 8*c*,*d*). The counter-rotating vortex contributes to an induced velocity on LEV2$_{ac}$ opposing the freestream, which results in the negative S_{xx} and $\langle \Omega_x \rangle \langle S_{xx} \rangle$ (observed in figure 9*d*). The intensified compression thus coincides with amplification of the spatial undulations, subsequently leading to localized annihilation and tearing of the LEV2$_{ac}$ core (see figure 8*d*).

Schaeffer & Le Dizés (2010) investigated the nonlinear evolution of the elliptic-type instability. They described an instability–breakdown–relaminarization mechanism, which characterized a lack of vortex core breakdown and an increase in its size on the convective time scale. This mechanism was also reported by Ryan *et al.* (2012), who numerically investigated the perturbation growth on unequal strength counter-rotating vortex pairs. The weaker vortex from the pair underwent breakdown to streamwise filaments, while the stronger primary vortex featured small-scale periodic stretching due to the presence of secondary streamwise filaments (Ryan *et al.* 2012). A similar mechanism is evident at $St_c = 0.32$, where the interaction of pre-existing hairpin-like structures with primary LEVs contributes to small-scale spanwise dislocations observed in figures 8(*a*) and 8(*b*). However, at $St_c = 0.40$, it is observed that besides the occurrence of vortex dislocations in the presence of hairpin-like structures that evolve from the secondary LEV (see figure 5), the primary TEV growth in proximity of the LEV results in localized intensification of compression. Thus the undulations continue to grow in amplitude, which eventually lead to transition from spanwise instability to its breakdown and formation of hairpin-like structures. This intensification of compression was not observed at $St_c = 0.32$ (see figures 9*a*,*b*). It also coincided with the absence of TEVs in neighbouring regions close to the primary LEV.

Similar to the evaluations at $St_c = 0.40$, the distribution of vortex compression in neighbouring regions upstream of LEV3$_{ac}$ is shown in figures 9(*e*) and 9(*f*) at $t^+ = 0.5$ and 0.75, respectively. The 'focus planes' are located along the span at $Z^+ = -0.625$ and 0.25 (see figures 8*e*,*f*). The advection of LEV3$_{ac}$ downstream coincides with temporal enhancement in vortex compression and the growth of TEV3$_c$ in its immediate proximity (see figure 9*f*). Figures 10(*e*) and 10(*f*) depict the quantitative profiles extracted along the axial direction (marked with green dashed lines in figures 9*c*,*d*). At $t^+ = 0.5$ in figure 10(*e*), $\langle \Omega_x \rangle \langle S_{xx} \rangle$ is approximately zero in neighbouring regions lying upstream of LEV3$_{ac}$. At $t^+ = 0.75$ in figure 10(*e*), however, the intensified compression is observed

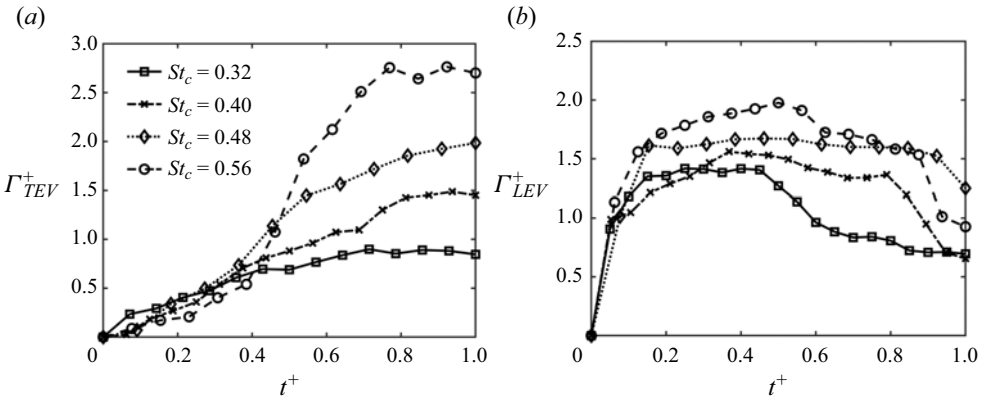

Figure 11. Variation of Γ^+_{TEV} and Γ^+_{LEV} at increasing St_c.

for $1.025 < X^+ < 1.07$, with a peak $\langle \Omega_x \rangle \langle S_{xx} \rangle$ corresponding to 0.4. A similar increase in compression is also apparent at $Z^+ = 0.25$ in figure 10(*f*). We note an increased compression upstream of LEV3$_{ac}$ (i.e. $X^+ < 1.04$) at $t^+ = 0.75$, compared to $t^+ = 0.5$, while the peak magnitude of $\langle \Omega_x \rangle \langle S_{xx} \rangle$ appears ahead of LEV3$_{ac}$ (i.e. $X^+ \approx 1.1$). This is an implication of the strong primary TEV core located slightly downstream of LEV3$_{ac}$ (evident in figure 9*f*). Besides the change in location of the peak $\langle \Omega_x \rangle \langle S_{xx} \rangle$ at $St_c = 0.48$, an overall consistency is observed in comparison to $St_c = 0.40$. Moreover, the observations at $St_c = 0.56$ are consistent with those at $St_c = 0.40$ and 0.48. These results are not presented, for brevity.

Besides associating the growth of TEVs with enhanced vortex compression around primary LEVs, it is worth noting that their circulation strength ($\Gamma^+ = \Gamma / U_\infty c$) increases in the range of St_c evaluated here. This is depicted in figure 11(*a*), where the accelerated increase in Γ^+_{TEV} is evident ahead of $t^+ = 0.4$. This finding supplements intensification of the $\langle S_{xx} \rangle$ magnitude discussed previously. This is therefore associated with the faster emergence of hairpin-like structures from the primary LEV with a magnified vortex compression reported earlier. Figure 11(*b*) also depicts the variation in Γ^+_{LEV} within one oscillation cycle at increasing St_c. The peak Γ^+_{LEV} clearly undergoes an increase with St_c that is supported by the fact that peak α_{eff} also depicts a similar trend as shown in figure 2. This also suggests that LEVs at higher St_c are more susceptible to the three-dimensional features and instability (Chiereghin *et al.* 2020; Son *et al.* 2022).

In addition to the vortex stretching and compression explained above, we also investigate vortex tilting that can further contribute to the transformation of spanwise vorticity in primary LEVs to streamwise vorticity in hairpin-like structures. Mathematically, vortex tilting is expressed as $\langle \Omega_y S_{xy} \rangle + \langle \Omega_z S_{xz} \rangle$. Figure 12 represents the qualitative and quantitative distribution of tilting for wake systems identified in the range of St_c evaluated here. The distribution is obtained on a *YZ*-plane in the vicinity of primary LEVs, ahead of which it experiences either a stagnation (i.e. at $St_c = 0.32$) or an amplification (i.e. at $St_c \geq 0.40$) in undulation amplitude. Similar to the observations discussed with respect to stretching/compression at $St_c = 0.32$, a decreased magnitude of tilting is observable at $t^+ = 0.75$, compared to $t^+ = 0.5$ (see figures 12*a–c*). At $t^+ = 0.5$, the spanwise slice depicts a peak positive magnitude of tilting at a localized region neighbouring the peak undulation bulge observable at $Z^+ \approx -0.25$ (see figure 12*a*). At $t^+ = 0.75$

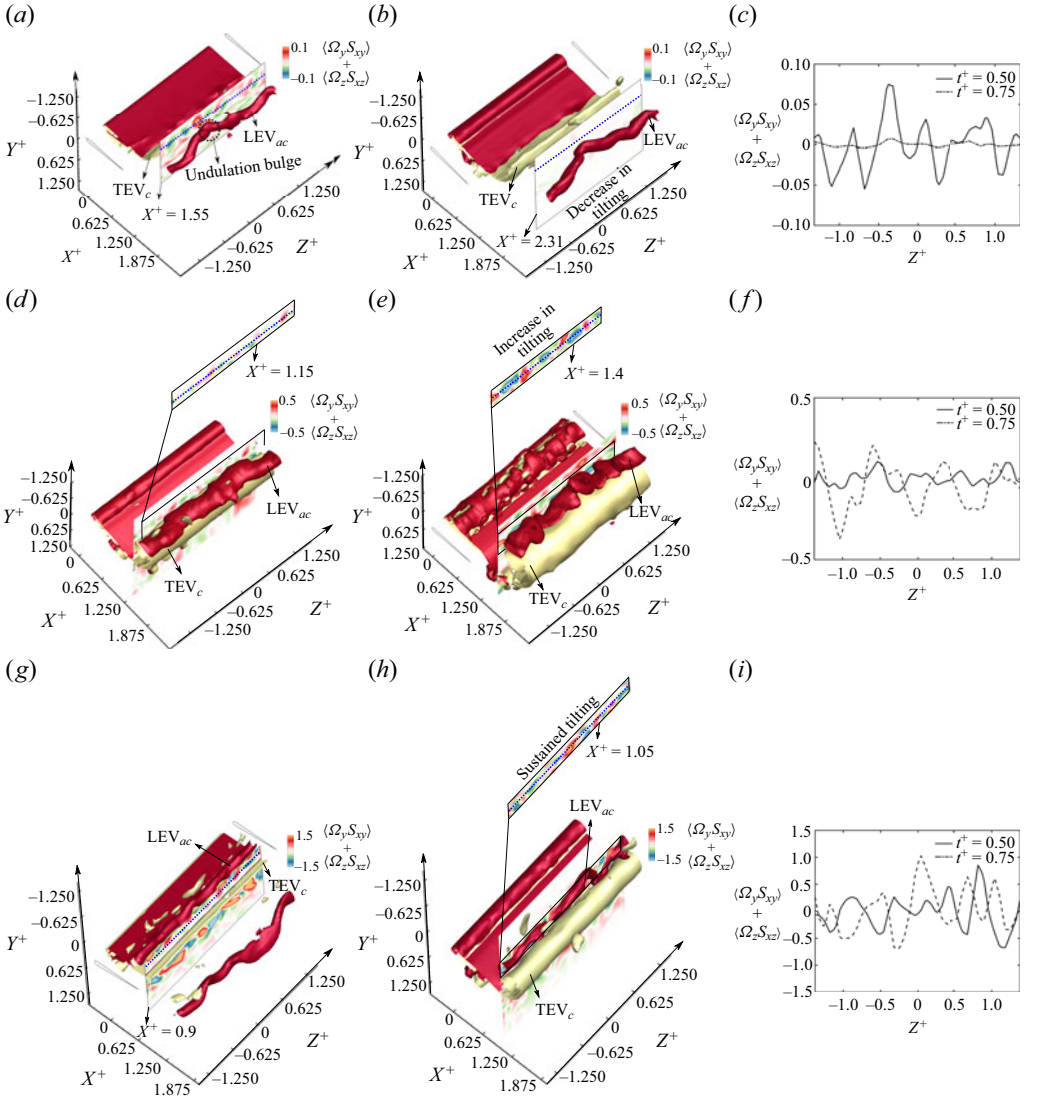

Figure 12. Distribution of $\langle \Omega_y S_{xy} \rangle + \langle \Omega_z S_{xz} \rangle$ at (*a–c*) $St_c = 0.32$, (*d–f*) $St_c = 0.40$ and (*g–i*) $St_c = 0.48$. The time instants are (*a*,*d*,*g*) $t^+ = 0.5$ and (*b*,*e*,*h*) $t^+ = 0.75$. (*c*,*f*,*i*) The extracted data on *YZ*-planes, with black solid and dashed lines marking contours of $\langle \Omega_y S_{xy} \rangle + \langle \Omega_z S_{xz} \rangle$.

(see figure 12*b*), the spanwise undulation of the primary LEV$_{ac}$ does not increase. This coincides with an apparent decrease in the distribution of tilting across the entire span region within the local vicinity of LEV$_{ac}$. The quantitative profiles (figure 12*c*) obtained on the spanwise slices at $t^+ = 0.5$ and 0.75 clearly demonstrate the decrease in vortex tilting.

Figures 12(*d–f*) depict qualitative snapshots of primary LEV and TEV structures for the wake system at $St_c = 0.40$. The distribution of $\langle \Omega_y S_{xy} \rangle + \langle \Omega_z S_{xz} \rangle$ along the spanwise slices at $t^+ = 0.5$ and 0.75 confirm an increase in the tilting magnitude as LEV$_{ac}$ advects downstream. Figures 12(*e*) and 8(*d*) also demonstrate the enhancement of spanwise undulation amplitude. Growth of the TEV in a closer proximity also coincides

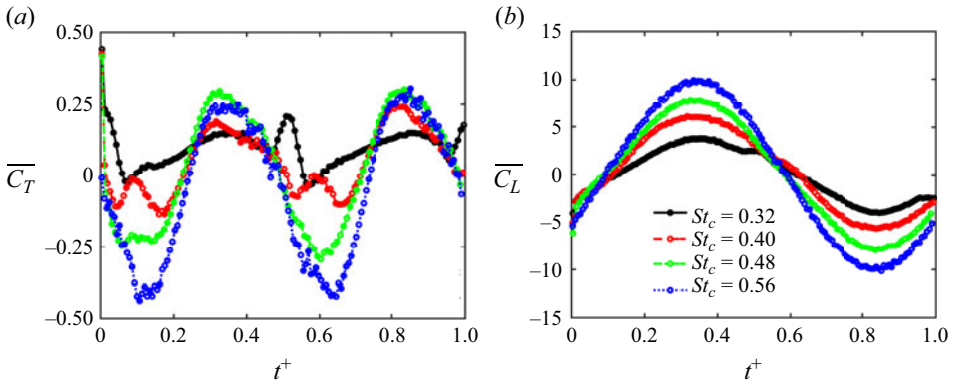

Figure 13. Temporal variation of $\overline{C_T}$ and $\overline{C_L}$ within one oscillation period of an oscillating foil at $\phi = 90^\circ$ and increasing St_c.

with an increase in the vortex tilting. A consistent trend is also observed at $St_c = 0.48$ (figures 12*g–i*), where magnitude of tilting increases at the spanwise slice at $t^+ = 0.75$. It is also clear that at $t^+ = 0.5$, a high magnitude of tilt is apparent in comparison to its distribution at lower St_c (see figures 12*c*,*f*). This links directly to the accelerated primary LEV bending reported earlier. It is well known that the hairpin-like coherent structures constitute a major streamwise vorticity component in the flow (Smith *et al.* 1991). As the bent primary LEV transforms to hairpin-like structures in the wake, tilting is found to be associated directly with the transformation of spanwise (LEV core) to streamwise (hairpin-like structures) vorticity.

3.4. *Influence of spanwise LEV instability transition on force generation*

Moriche *et al.* (2016) investigated and reported the association of vortex instability and force generation behind foils oscillating in combined heaving and pitching motion. Here, we perform a similar assessment in order to understand if the transition in spanwise LEV instability to the secondary hairpin-like structure in the wake impacts the force variation of oscillating foils. Figures 13(*a*) and 13(*b*) depict the variation of the coefficients of thrust ($\overline{C_T}$) and lift ($\overline{C_L}$) over a single period of oscillation, at $\phi = 90^\circ$ and increasing St_c. The variation of $\overline{C_T}$ in figure 13(*a*) depicts a period doubling behaviour at $St_c \leq 0.40$. This is associated with the shedding of an LEV–TEV pair in the wake, which resembles a $2P$ wake topology, as explained by Verma & Hemmati (2022*a*). As St_c increases beyond 0.40, the period doubling behaviour is lost in $\overline{C_T}$ variation, which coincides with an accelerated transformation of LEVs to secondary hairpin-like structures. The $\overline{C_L}$ distribution in figure 13(*b*) does not demonstrate a substantial change with St_c. The increasing magnitude of maxima occurs on account of the increase in LEV circulation at increasing St_c, as reported in Verma *et al.* (2023). In terms of the propulsive performance, table 2 depicts the time-averaged C_T and $C_{L,rms}$ over one oscillation period. Overall, the range of St_c between 0.32 and 0.48 presents a drag-dominated performance, while a low thrust generation is observed for $St_c = 0.56$. This is consistent with the findings of Van Buren *et al.* (2019).

St_c	$\overline{C_T}$	$C_{L,rms}$
0.32	0.0953	2.5833
0.40	0.0475	4.0418
0.48	0.0230	5.3680
0.56	−0.0464	6.8680

Table 2. Computed $\overline{C_T}$ and $C_{L,rms}$ of an oscillating foil at $\phi = 90^\circ$ and increasing St_c.

4. Conclusions

Transition of spanwise instability on primary leading edge vortex (LEV) rollers towards the formation of hairpin-like structures is observed in the wake of an oscillating foil with increasing St_c in the range $0.32 \leq St_c \leq 0.56$. This system of secondary hairpin-like vortical structures grows in conjunction with the previously identified hairpin-like pairs that evolve from the core vorticity outflux of deforming secondary LEVs (Verma & Hemmati 2023; Verma *et al.* 2023). At $St_c = 0.32$, vortex undulations and spanwise dislocations do not reveal temporal amplification, and hence fail transition to another system of hairpin-like vortical structures. However, beyond $St_c = 0.32$, undulations amplify with advection of the LEV in the wake, which subsequently coincides with vortex tearing at localized spanwise locations along the roller. Hence the LEV itself transforms to the hairpin-like system that evolves in conjunction with the pre-existing hairpin-like structures. The amplification of undulations at $St_c > 0.32$ is associated with enhanced vortex compression and tilting around the upstream regions neighbouring primary LEVs. This also coincides with the presence and growth of counter-rotating trailing edge vortices (TEVs) that only act as a source for intensifying axial strain fields, while having no contribution in the onset of spanwise instability on the primary LEV. The increasing circulation of TEVs at higher St_c further accelerates the intensification of compression, which coincides with an early growth of secondary hairpin-like system from the primary LEV.

Funding. This research has received support from the Canada First Research Excellence Grant. The computational analysis was completed using Compute Canada clusters.

Declaration of interests. The authors report no conflict of interest.

Author ORCIDs.
Suyash Verma https://orcid.org/0000-0001-6395-2533;
Arman Hemmati https://orcid.org/0000-0002-8897-4525.

Author contributions. Authors may include details of the contributions made by each author to the paper.

References

ANDERSEN, A., BOHR, T., SCHNIPPER, T. & WALTHER, J.H. 2017 Wake structure and thrust generation of a flapping foil in two-dimensional flow. *J. Fluid Mech.* **812**, R4.

ANDERSON, J.M., STREITLIEN, K., BARRETT, D.S. & TRIANTAFYLLOU, M.S. 1998 Oscillating foils of high propulsive efficiency. *J. Fluid Mech.* **360**, 41–72.

BARKLEY, D. & HENDERSON, R.D. 1996 Three-dimensional Floquet stability analysis of the wake of a circular cylinder. *J. Fluid Mech.* **322**, 215–241.

BILBAO-LUDENA, J.C. & PAPADAKIS, G. 2023 Structure of vorticity and turbulence fields in a separated flow around a finite wing: analysis using direct numerical simulation. *Phys. Rev. Fluids* **8** (1), 014704.

BREDE, M., ECKELMANN, H. & ROCKWELL, D. 1996 On secondary vortices in the cylinder wake. *Phys. Fluids* **8** (8), 2117–2124.

BRISTOL, R.L., ORTEGA, J.M., MARCUS, P.S. & SAVAS, Ö. 2004 On cooperative instabilities of parallel vortex pairs. *J. Fluid Mech.* **517**, 331–358.

BULL, S., CHIEREGHIN, N., GURSUL, I. & CLEAVER, D.J. 2021 Unsteady aerodynamics of a plunging airfoil in transient motion. *J. Fluids Struct.* **103**, 103288.

CALDERON, D.E., CLEAVER, D.J., GURSUL, I. & WANG, Z. 2014 On the absence of asymmetric wakes for periodically plunging finite wings. *Phys. Fluids* **26** (7), 071907.

CHIEREGHIN, N., BULL, S., CLEAVER, D.J. & GURSUL, I. 2020 Three-dimensionality of leading-edge vortices on high aspect ratio plunging wings. *Phys. Rev. Fluids* **5**, 064701.

CROW, S.C. 1970 Stability theory for a pair of trailing vortices. *AIAA J.* **8** (12), 2172–2179.

DENG, J. & CAULFIELD, C.P. 2015 Three-dimensional transition after wake deflection behind a flapping foil. *Phys. Rev.* E **91** (4), 043017.

DENG, J., SUN, L., LUBAO, T., PAN, D. & SHAO, X. 2016 The correlation between wake transition and propulsive efficiency of a flapping foil: a numerical study. *Phys. Fluids* **28** (9), 094101.

FLORYAN, D., VAN BUREN, T., ROWLEY, C.W. & SMITS, A.J. 2017 Scaling the propulsive performance of heaving and pitching foils. *J. Fluid Mech.* **822**, 386–397.

GIBEAU, B., KOCH, C.R. & GHAEMI, S. 2018 Secondary instabilities in the wake of an elongated two-dimensional body with a blunt trailing edge. *J. Fluid Mech.* **846**, 578–604.

HEMMATI, A., VAN BUREN, T. & SMITS, A.J. 2019 Effects of trailing edge shape on vortex formation by pitching panels of small aspect ratio. *Phys. Rev. Fluids* **4**, 033101.

KIM, D., STROM, B., MANDRE, S. & BREUER, K. 2017 Energy harvesting performance and flow structure of an oscillating hydrofoil with finite span. *J. Fluids Struct.* **70**, 314–326.

LEWEKE, T., LE DIZÈS, S. & WILLIAMSON, C.H.K. 2016 Dynamics and instabilities of vortex pairs. *Annu. Rev. Fluid Mech.* **48**, 507–541.

LEWEKE, T. & WILLIAMSON, C.H.K. 1998 Cooperative elliptic instability of a vortex pair. *J. Fluid Mech.* **360**, 85–119.

MEUNIER, P. & LEWEKE, T. 2005 Elliptic instability of a co-rotating vortex pair. *J. Fluid Mech.* **533**, 125–159.

MITTAL, R. & BALACHANDAR, S. 1995 Generation of streamwise vortical structures in bluff body wakes. *Phys. Rev. Lett.* **75** (7), 1300–1303.

MORICHE, M., FLORES, O. & GARCÍA-VILLALBA, M. 2016 Three-dimensional instabilities in the wake of a flapping wing at low Reynolds number. *Intl J. Heat Fluid Flow*. **62** (Part A), 44–55.

MUELLER, T.J. & DELAURIER, J.D. 2003 Aerodynamics of small vehicles. *Annu. Rev. Fluid Mech.* **35** (1), 89–111.

NAZARINIA, M., LO JACONO, D., THOMPSON, C.M. & SHERIDAN, J. 2009 The three-dimensional wake of a cylinder undergoing a combination of translational and rotational oscillation in a quiescent fluid. *Phys. Fluids*. **21** (6), 064101.

ORTEGA, J.M., BRISTOL, R.L. & SAVAS, Ö. 2003 Experimental study of the instability of unequal-strength counter-rotating vortex pairs. *J. Fluid Mech.* **474** (474), 35–84.

ORTEGA, J.M. & SAVAS, O. 2001 Rapidly growing instability mode in trailing multiple-vortex wakes. *AIAA J.* **39** (4), 750–754.

PETRA, T. 2019 Description of the overset mesh approach in ESI version of OpenFOAM. In *Proceedings of the CFD with OpenSource Software* (ed. H. Nilsson). Chalmers University of Technology.

RYAN, K., BUTLER, C.J. & SHEARD, G.J. 2012 Stability characteristics of a counter-rotating unequal-strength Batchelor vortex pair. *J. Fluid Mech.* **696**, 374–401.

RYAN, K., THOMPSON, M.C. & HOURIGAN, K. 2005 Three-dimensional transition in the wake of bluff elongated cylinders. *J. Fluid Mech.* **538**, 1–29.

SCHAEFFER, N. & LE DIZÉS, S. 2010 Nonlinear dynamics of the elliptic instability. *J. Fluid Mech.* **646**, 471–480.

SENTURK, U. & SMITS, A.J. 2019 Reynolds number scaling of the propulsive performance of a pitching airfoil. *AIAA J.* **57**, 2663–2669.

SMITH, C.R., WALKER, J.D.A., HAIDARI, A.H. & SOBRUN, U. 1991 On the dynamics of near-wall turbulence. *Phil. Trans. R. Soc. Lond.* A **336** (1641), 131–175.

SMITS, A.J. 2019 Undulatory and oscillatory swimming. *J. Fluid Mech.* **874**, P1.

SON, O., GAO, A.-K., GURSUL, I., CANTWELL, C.D., WANG, Z. & SHERWIN, S.J. 2022 Leading-edge vortex dynamics on plunging airfoils and wings. *J. Fluid Mech.* **940**, A28.

SUN, L., DENG, J. & SHAO, X. 2018 Three-dimensional instabilities for the flow around a heaving foil. *Phys. Rev.* E **97** (1), 013110.

TALBOYS, E., GEYER, T.F., PRÜFER, F. & BRÜCKER, C. 2021 A parametric study of the effect of self-oscillating trailing-edge flaplets on aerofoil self-noise. *Appl. Acoust.* **177**, 107907.
TRIANTAFYLLOU, M.S., HOVER, F.S., TECHET, A.H. & YUE, D.K.P. 2005 Review of hydrodynamic scaling laws in aquatic locomotion and fishlike swimming. *Appl. Mech. Rev.* **58**, 226–237.
VAN BUREN, T., FLORYAN, D. & SMITS, A.J. 2019 Scaling and performance of simultaneously heaving and pitching foils. *AIAA J.* **57**, 3666–3677.
VERMA, S., FREEMAN, B.R.S. & HEMMATI, A. 2022 Effects of Reynolds number and average angle of attack on the laminar scaling of oscillating foils. *Phys. Fluids* **34** (3), 031905.
VERMA, S. & HEMMATI, A. 2020 Performance of overset mesh in modeling the wake of sharp-edge bodies. *Computation*. **8** (3), 66.
VERMA, S. & HEMMATI, A. 2021 Evolution of wake structures behind oscillating hydrofoils with combined heaving and pitching motion. *J. Fluid Mech.* **927**, A23.
VERMA, S. & HEMMATI, A. 2022*a* Characterization of bifurcated dual vortex streets in the wake of an oscillating foil. *J. Fluid Mech.* **945**, A7.
VERMA, S. & HEMMATI, A. 2022*b* Route to transition in propulsive performance of oscillating foil. *Phys. Rev.* E **105** (4), 045102.
VERMA, S. & HEMMATI, A. 2023 Influence of kinematics on the growth of secondary wake structures behind oscillating foils. *Intl J. Heat Fluid Flow* **102**, 109146.
VERMA, S., KHALID, M.S.U. & HEMMATI, A. 2023 On the association of kinematics, spanwise instability and growth of secondary vortex structures in the wake of oscillating foils. *Proc. R. Soc.* A **479**, 2276.
VERMA, S., KHALID, M.S.U. & HEMMATI, A. 2024 Stability of secondary vortex evolution in wake of oscillating foils. *Phys. Fluids* **36** (6), 064106.
VISBAL, M.R. 2009 High-fidelity simulation of transitional flows past a plunging airfoil. *AIAA J.* **47**, 11.
VISBAL, M.R. 2012 Numerical investigation of deep dynamic stall of a plunging airfoil. *AIAA J.* **49** (10), 2152–2170.
WANG, Q., ZHAO, Q. & WU, Q. 2015 Aerodynamic shape optimization for alleviating dynamic stall characteristics of helicopter rotor airfoil. *Chin. J. Aeronaut.* **28** (2), 346–356.
WILLIAMSON, C.H.K. 1996 Three-dimensional wake transition. *J. Fluid Mech.* **328**, 345–407.
WU, J.-Z., MA, H.-Y. & ZHOU, M.-D. 2006 *Vorticity and Vortex Dynamics*. Springer.
ZHANG, D. & HUANG, W.X. 2023 Hydrodynamics of a swimming batoid fish at Reynolds numbers up to 148 000. *J. Fluid Mech.* **963**, A16.
ZURMAN-NASUTION, A.N., GANAPATHISUBRAMANI, B. & WEYMOUTH, G.D. 2020 Influence of three-dimensionality on propulsive flapping. *J. Fluid Mech.* **886**, A25.